

Measurement of diffractive Central Exclusive Production of $h\bar{h}$ pairs $(h=\pi,K,p)$ in proton-proton collisions at $\sqrt{s}=200$ GeV with forward proton reconstruction in Roman Pot detectors

Leszek Adamczyk, Łukasz Fulek, Mariusz Przybycień, and Rafał Sikora

AGH University of Science and Technology, FPACS, Kraków, Poland

February 1, 2019

Abstract

In this note we present analysis of diffractive Central Exclusive Production using 2015 data from proton-proton collisions at $\sqrt{s}=200$ GeV. This dataset was collected with newly installed Roman Pot detectors in Phase II* configuration which ensured efficient triggering and measuring diffractively scattered protons. We describe intermediate stages of analysis involving choice of selection cuts, comparison of data with Monte Carlo models folded into detector acceptance, and study of systematic uncertainties specific to the analysis. Finally, we show the physics outcome of the analysis. Parts of the analysis which are of more technical nature (calculation of efficiencies, derivation of corrections to efficiencies, adjustment of the STAR simulation, systematic uncertainty of efficiencies) are described in a supplementary analysis note [1].

Contents

Lis	of contributions	4
Ch	ange log	4
1	Introduction 1.1 Central Exclusive Production	5 . 6 . 6
2	Data set 2.1 Trigger	. 8
3	Event selection 3.1 List of cuts 3.2 Description of cuts 3.2.1 (C1,C2) Primary vertex and its z-position 3.2.2 (C3) TPC tracks 3.2.3 (C4) RP tracks 3.2.4 (C5) TPC-RP z-vertex matching 3.2.5 (C6) BBC-large signal veto 3.2.6 (C7) TOF clusters limit 3.2.7 (C8) Exclusivity cut (missing p_T cut) 3.2.8 (C9) Particle identification 3.3 Working point for cuts C6, C7 and C8 3.4 Signal per integrated luminosity 3.5 Cut flow	. 10 . 10 . 10 . 15 . 15 . 16 . 16 . 17 . 18 . 20
4	Corrections 1.1 Method of corrections application	22 22 23 23 23 23 23 23 23 23 23 23 23 2

	4.5	Unfolding	24
5	5.1	Sources of background	$\frac{25}{25}$
6		Relative normalization of background and signal	26 27
7	Phys	sics results	28
Li	st of	Figures	33
Li	st of	Tables	33
\mathbf{R}_{0}	eferer	nces	34

List of contributions

Leszek Adamczyk	Analysis coordination/supervision, production of picoDST, production of embedded MC samples
Łukasz Fulek	Analysis support
Mariusz Przybycień	Analysis supervision
Rafał Sikora*	Main analyzer

 $^{^\}star$ - contact editor

Change log

?? Feb 2019	ver. 1.0	Initial revision		

1. Introduction

1.1 Central Exclusive Production

The Central Exclusive Production (CEP) takes place when interacting particles form a state in the mid-rapidity region ("central production") whose all constituents/decay products are measured in the detector ("exclusive"). The initial state particles can either dissociate, excite or stay intact. The latter case of CEP in proton-proton collisions can be written as

$$p + p \rightarrow p + X + p$$
 (1.1)

and depicted as in Fig. 1.1. Mass and rapidity of state X is given by

$$M_X = \sqrt{s(\xi_1 \xi_2 \sin^2(\alpha/2) - (1 - \xi_1 - \xi_2) \cos^2(\alpha/2))} \stackrel{\alpha = \pi}{=} \sqrt{s\xi_1 \xi_2}, \quad (1.2) \qquad y_X = \frac{1}{2} \ln \frac{\xi_1}{\xi_2}, \quad (1.3)$$

where α is angle between scattered protons and $\xi = (p_0 - p)/p_0$ is the fractional momentum loss of proton.

1.2 Double IPomeron Exchange

Reaction from Eq. (1.1) can exhibit purely electromagnetic (γ - γ interaction), mixed (γ - \mathcal{O} interaction) or purely strong nature (\mathcal{O} - \mathcal{O} interaction). The last type is dominant at RHIC energies. It is characterized by the lack of hard scale (if protons are scattered at small angles), therefore perturbative QCD cannot be applied and Regge theory [2] is used instead. An object \mathcal{O} does not have unequivocal QCD representation - in Regge formalism it is the so-called "trajectory" (Reggeon, \mathbb{R}). Reggeon with quantum numbers of vacuum is called "Pomeron" (\mathbb{P}) and \mathbb{P} - \mathbb{P} reaction (Fig. 1.2) is called "Double Pomeron Exchange".

Processes involing IPomeron exchange are referred as diffraction due to cross-section in scattering angle resembling similar shape to insteady pattern of diffracted light. For low values of Mandelstam t (small scattering angles) cross-section takes exponential form

$$\frac{d\sigma}{d|t|} \propto e^{-B|t|},\tag{1.4}$$

where the slope parameter B reflects the size of target at which \mathbb{P} omerons scatter.

Diffractive events have specific property of the "rapidity gap" which is an angular region free of hadrons. In DIPE two such gaps are present, marked in Fig. 1.1 as $\Delta \eta_1$ and $\Delta \eta_2$.

DIPE is a spin-parity filter - the fact that scattered particles have all quantum numbers unchanged after the interaction, production of central states satisfying Eq. (1.5) is enhanced

$$I^G J^{PC} = 0^+ \text{even}^{++}.$$
 (1.5)

The lowest order QCD picture of the Pomeron is a pair of oppositely colored gluons (colour singlet). This fact makes the DPE recognized as the gluon-rich environment process in which bound states of gluons ("glueballs") or hybrid mesons could be preferably produced.

For detailed introduction to the topic of diffraction see Refs. [3,4].

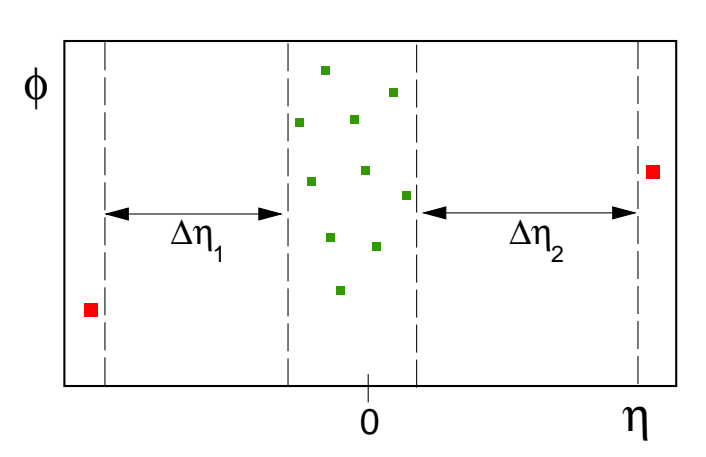


Figure 1.1: CEP represented in η - ϕ space.

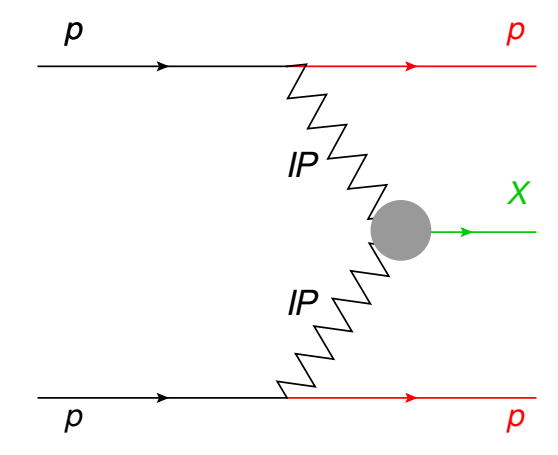


Figure 1.2: Diagram of DIPE process.

1.3 Physics motivation for the measurement

STAR collected in 2015 large dataset dedicated for measurement of the Central Diffraction (DIPE in particular). Since that year the experiment was enriched with Roman Pot Phase II* subsystem and thus gained possibility of detection of forward protons. It enabled studies of properties of the central state with respect to observables related to exchanged IPomerons. No such measurement was performed before at that high c.m.s. energy ($\sqrt{s} = 200$ GeV, contamination from IReggeon exchanges is small) which makes it particularly attractive. A brief list of physics issues that can be covered with the study described in this note is briefly introduced below.

1.3.1 DIPE differential cross-sections, mass spectrum

As stated in Sec. 1.2 DIPE is a soft process whose theoretical description is done mainly using phenomenological tools, thus measurement of differential cross-sections is needed to verify various production models.

The main focus is put on the simplest state (and most numerously) produced in DPE, namely a pair of oppositely charged pions, $\pi^+\pi^-$. It can be formed either in a non-resonant or resonant mechanism. In the first case the $\pi^+\pi^-$ continuum is formed by the exchange of the off-shell pion between Pomerons. Currently there are two models of this reaction on the market [5,6], [7]. In the second case the Pomerons directly couple into resonance (e.g. $f_2(1270)$), which then decays to $\pi^+\pi^-$. Attempts to calculate cross-section for this production mechanism are presented in Ref. [6] and [8].

Understanding of the mass spectrum in $\pi^+\pi^-$ channel is important to learn about relative contribution from continuum and resonant production, as well as relative production of resonances. Recognition of resonant states may indicate candidates for low-mass glueballs of $J^{PC}=0^{++}$, however presence of underlaying scalar $q\bar{q}$ states makes this task challenging.

Other channels, like K^+K^- , are also of great interest. Comparison of the cross-sections for production of $\pi^+\pi^-$ and K^+K^- gives information about strength of the Pomeron coupling to different quark flavors. Also, structures in $d\sigma/dm$ can be easier attributed to resonances by measuring more than one channel and known branching ratios thereof.

Detection of intact protons scattered at very small angle with respect to the beamline enables determination of the reaction plane which makes the Partial Wave Analysis (PWA) possible. It also allows to look at the the cross-sections more differentially, especially with respect to properties of exchanged Pomerons, like carried squared four-momentum t, azimuthal separation of Pomerons in the transverse plane $\Delta \varphi$ or relative momentum of Pomerons Δp_T . The last quantity was proposed to distinguish pure $q\bar{q}$ states from these with gluonic content [9].

1.3.2 Absorption effects

One can imagine in diagram in Fig. 1.2 additional soft lines e.g. between protons in the initial state or one of Pomerons and final state proton. These so-called rescattering effects (or absorption effects) lead to production of hadrons other than these belonging to central state X hence the diffractive signature of an event in form of rapidity gap is no longer present. Measurement of the probability that the state X will remain exclusive and forward protons will remain intact, in other words the rapidity gap survival probability S^2 , would be valuable ingredient for development of absorption models.

1.3.3 Size of interaction region

From the measurement of protons in Roman Pots one is able to reconstruct squared four-momenta transferred in proton-Pomeron vertices and determine the differential cross-section $d\sigma/d|t|$. Fit of exponent allows to extract the slope parameter B, which may depend on the Pomeron-Pomeron c.m.s. energy, or in other words on the mass of diffractive system X. Knowledge on the slope parameter gives insight to the form factor of the object at which Pomeron scatters.

2. Data set

2.1 Trigger

The main trigger designed for studies of Central Diffraction in run 15 was RP_CPT2. It was formed of the following conditions combined by logical AND (&&):

- 1. (ET && !IT) || (!ET && IT) = signal in at least one RP on each side of the STAR central detector to ensure presence of two forward-scattered protons; a veto was imposed on simultaneous signal in RPs above and below the beamline, which might have originated either from proton dissociation, or pile-up event, or beam halo proton etc.,
- 2. !BBCE && !BBCW && !ZDCE && !ZDCW = veto on any signal in small BBC tiles or ZDCs on any side of STAR central detector such requirement is in accordance with the double-gap topology of CEP events, it mostly filtered out CEP events with parallel pile-up event(s),
- 3. $TOF \ge 2$ = at least 2 hits in TOF aim of this condition was to ensure activity in the mid-rapidity; since the lowest multiplicity allowed in CEP is 2, that was the lower threshold of L0 TOF multiplicity.

This trigger was running with an average prescale of 5 and average DAQ rate of 250 Hz, which allowed to collect in total about 560 M events corresponding to 16.5 pb⁻¹ of integrated luminosity. More information about number of events per run, rates etc. can be found under link provided in Ref. [10], which contains selected data from STAR run log [11]. Luminosity data used in this analysis comes from Ref. [12].

All RP triggers which were intended for usage in diffractive physics analyses or efficiency studies are listed in Tab. 2.1. Components used in definitions of these triggers are outlined in Fig. 2.1. Detailed explanation of all trigger bits can be found in Refs. [13,14]. Explanation of naming convention in Roman Pot system can be found in Ref. [15].

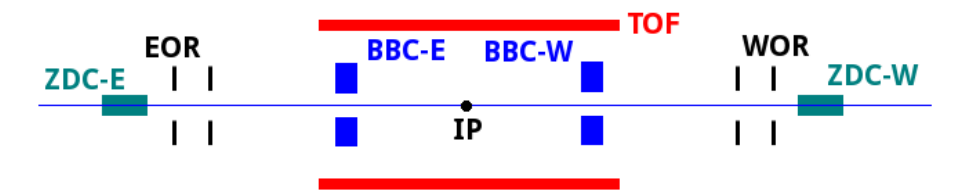


Figure 2.1: Sketch of the trigger components used in definitions of diffractive triggers in run 15.

Trigger name	Definition	Events [M]	Comment
RP_CP	EOR && WOR	73.3	Loose trigger (mostly elastic events) designed for monitoring/trigger efficiency study
RP_CPT	EOR && WOR && !BBCE && !BBCW && !ZDCE && !ZDCW && TOF≥1	38.9	Intended to be main CEP trigger (later switched to RP_CPT2 due to large prescale)
RP_CPT2	(ET && !IT) (!ET && IT) && !BBCE && !BBCW && !ZDCE && !ZDCW && TOF≥2	556.5	Main CEP trigger Note: On Apr 14 added upper TOF limit (10)
RP_CPX	IT && !BBCE && !BBCW && !ZDCE && !ZDCW && TOF≥2	40.1	The same as RP_CPT2 but only IT configuration
RP_CPEI	ET && IT && !BBCE && !BBCW && !ZDCE && !ZDCW && TOF>2	15.6	Control trigger for CPT2 to estimate effect of !(ET && IT) veto

Table 2.1: Central Diffraction physics triggers and control triggers involving Roman Pot detectors in run 15.

2.2 Reconstruction software

Raw data was processed with STAR libraries in versions SL17f. All four trigger datasets were processed: production_pp200trans_2015, production_pp200long2_2015, production_pp200long3_2015 and production_pp200long_2015 (see [16]).

The following BFC options were used in the reconstruction:

DbV20160418,pp2015c,btof,mtd,mtdCalib,pp2pp,-beamline,beamline3D,useBTOFmatchOnly,VFStoreX,fmsDat,fmsPoint,fpsDat,BEmcChkStat,-evout,CorrX,OSpaceZ2,OGridLeak3D,-hitfilt

Main attention should be put on option **useBTOFmatchOnly** which forced vertexing algorithm to form vertices only from the global TPC tracks which are matched with hits in the TOF system. This solution was found to yield significantly larger signal reconstruction efficiency (vertexing efficiency) and better resolutions. The study which lead to above conclusions, presented in Ref. [17], was performed on the same dataset processed with older libraries SL15k (without useBTOFmatchOnly option).

2.3 Data format

The analyzed data was stored in ROOT files in the picoDST format which was in large part a skimmed MuDST (standard STAR format). The picoDST format was introduced in Ref. [18]. PicoDST description files (C++ headers etc.) can be found in the analysis code repository [19].

3. Event selection

Complete list of analysis cuts used for signal extraction is presented in Sec. 3.1. Detailed description of each cut can be found in Sec. 3.2.

List of cuts¹ 3.1

- C1. Exactly 1 primary vertex with TPC track(s) matched with hits in TOF.
- C2. TPC vertex from C1 is placed within $|z_{vx}| < 80$ cm.
- C3. Exactly 2 opposite-sign primary TPC tracks (C3.2) of good quality (C3.4) matched with hits in TOF (C3.1), reconstructed within kinematic region of high TPC acceptance (C3.3) and with small distance of closest approach (DCA) to the vertex (C3.5).
 - C3.1. Exactly 2 TOF-matched (match flag > 0) primary tracks and no additional primary tracks matched with BEMC clusters,
 - C3.2. Tracks are of opposite signs,
 - C3.3. Both tracks are contained within the kinematic range:

$$|\eta| < 0.7, \quad p_T > 0.2 \text{ GeV}/c,$$

C3.4. Both tracks satisfy quality criteria:

$$N_{
m hits}^{
m fit} \geq 25, \quad N_{
m hits}^{
m dE/dx} \geq 15, \quad |d_0| < 1.5 \ {
m cm},$$

C3.5. Both tracks match well to the primary vertex:

$$DCA(R) < 1.5 \text{ cm}, \quad DCA(z) < 1 \text{ cm}.$$

- C4. Exactly 1 RP track on each side of STAR central detector (C4.3) of good quality (C4.1), with local angles consistent with the IP being the track origin (C4.2), lying within fiducial region of high geometrical acceptance (C4.4).
 - C4.1. RP tracks contain only track-points with at least 3 (out of 4) planes used in reconstrucion,
 - C4.2. Local angles $(\theta_x^{\text{RP}}, \theta_u^{\text{RP}})$ consistent with expectation for protons originating from the IP

$$-2 \; \mathrm{mrad} < \theta_x^{\mathrm{RP}} - x^{\mathrm{RP}}/|z^{\mathrm{RP}}| < 4 \; \mathrm{mrad}, \qquad -2 \; \mathrm{mrad} < \theta_y^{\mathrm{RP}} - y^{\mathrm{RP}}/|z^{\mathrm{RP}}| < 2 \; \mathrm{mrad},$$

- C4.3. Exactly 1 track passing cuts C4.1-C4.2 per side,
- **C4.4**. Tracks passing cut C4.3 lie within the fiducial (p_x, p_y) region defined as:

$$0.2 < |p_y| < 0.4$$
, $-0.2 < p_x$, $(p_x + 0.3)^2 + p_y^2 < 0.5^2$ (all in GeV).

- C5. Vertex z-positions measured in TPC and reconstructed from the difference of proton detection time in west and east RPs are consistent with each other within the resolution: $|z_{\text{vx}}^{\text{TPC}} z_{\text{vx}}^{\text{RP}}| < 36 \text{ cm } (3\sigma_{\Delta z_{\text{vtx}}})$.
- C6. No signal in any tile of BBC-large (east or west) with ADC > ADC_{thr} and 100 < TDC < 2400, where ADC_{thr} is specific for each channel.
- C7. Maximally 3 reconstructed TOF clusters $N_{\rm clstrs}^{\rm TOF} \leq 3$.
- C8. Missing (total) momentum of TPC tracks and RP tracks $p_T^{\text{miss}} < 75 \text{ MeV}/c$.
- C9. Particle (pair) identification:

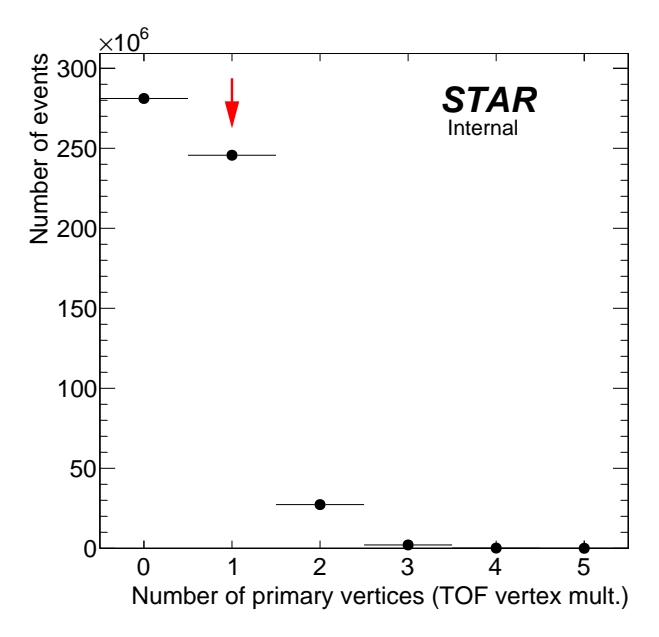
Particle (pair) identification: if
$$n\sigma_{\mathrm{pion}}^{\mathrm{pair}} > 3$$
 & $n\sigma_{\mathrm{kaon}}^{\mathrm{pair}} > 3$ & $n\sigma_{\mathrm{proton}}^{\mathrm{pair}} < 3$ & $m_{\mathrm{TOF}}^{2} > 0.6 \; \mathrm{GeV}/c^{2} \rightarrow pp$ elif $n\sigma_{\mathrm{pion}}^{\mathrm{pair}} > 3$ & $n\sigma_{\mathrm{kaon}}^{\mathrm{pair}} < 3$ & $n\sigma_{\mathrm{proton}}^{\mathrm{pair}} > 3$ & $m_{\mathrm{TOF}}^{2} > 0.15 \; \mathrm{GeV}/c^{2} \rightarrow KK$ elif $|n\sigma_{\mathrm{pion}}^{\mathrm{trk}}| < 3$ & $|n\sigma_{\mathrm{pion}}^{\mathrm{trk}}| < 3$ $\pi\pi$ else event rejected.

¹Some cuts (e.g. C3) are decomposed to constituent sub-cuts. Cut is formed by the logical AND of all its sub-cuts.

3.2 Description of cuts

3.2.1 (C1,C2) Primary vertex and its z-position

As it was designed in the trigger logic, we aim to perform CEP analysis in a clean, pile-up-free environment, therefore we cut on primary vertex multiplicty (Fig. 3.1) to reject events with more than one interaction per bunch crossing. We require exactly one primary vertex containing TPC tracks matched with hits in TOF (matching of the track with hit in TOF is identified with the TOF match flag being different from 0). Later in the text we refer to such events as a single "TOF vertex" events.



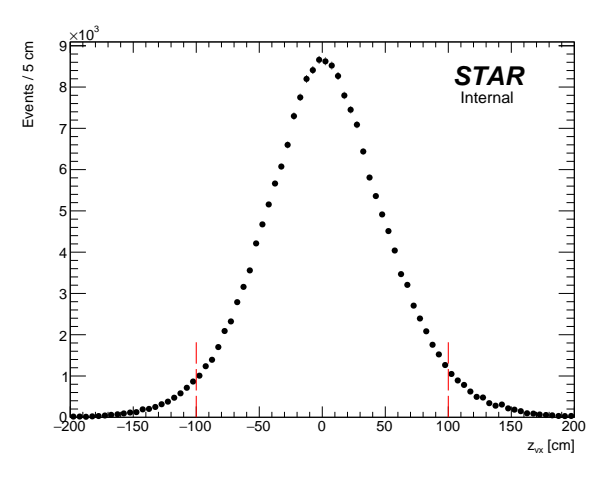


Figure 3.1: Primary vertex multiplicty. Red arrow marks bin with events with exactly one primary vertex (with track(s) matched with hit in TOF), which are used in physics analysis.

Figure 3.2: z-position of the primary vertex in single TOF vertex events. Red dashed line indicate range of longitudinal vertex position accepted in analysis.

The single TOF vertex is required to be placed within a range (-80 cm, 80 cm) along the z-axis (Fig. 3.2). Events with vertices away from the nominal IP have low acceptance both for the central tracks and the forward protons (comparing to events with vertices close to nominal IP), therefore we reject them as their inclusion to analysis would naturally introduce large systematic uncertainties. See Sec. 3.2.3 in Ref. [1]

3.2.2 (C3) TPC tracks

The TPC track selection starts from the selection of events with exactly two primary tracks matched with hit in TOF (Fig. 3.3). Matching with TOF guarantee that analyzed tracks originate from the triggered bunch crossing (ensures that tracks are "in-time"). It is in accordance with the trigger logic which required at least 2 L0 TOF hits, as well as it enables more accurate particle identification with merged time-of-flight and dE/dx method, comparing to sole usage of dE/dx. Primary tracks not matched with hit in TOF, whose average multiplicty in single TOF vertex is \sim 8, are hardly distinguished between real and fake (off-time) tracks, which is an additional reason for not analyzing events with only one TOF-matched primary TPC track (the other track might be unmatched due to TOF inefficiency).

Primary TPC tracks from the single TOF vertex which are matched with TOF are allowed to be also matched with BEMC clusters. Matching with BEMC cluster is claimed if the distance in $\eta - \phi$ space between the BEMC cluster position ($\eta_{\rm clus}$, $\phi_{\rm clus}$) and projected position of the track in BEMC ($\eta_{\rm proj}$, $\phi_{\rm proj}$), defined as

$$R = \sqrt{(\eta_{\text{clus}} - \eta_{\text{proj}})^2 + (\phi_{\text{clus}} - \phi_{\text{proj}})^2},$$
(3.1)

is less than $R_{\text{max}}^{\text{match}} = 0.05$. Distribution of the distance between the primary TPC track and the closest BEMC cluster is shown in Fig. 3.4.

However, if there are any primary TPC tracks matched with BEMC cluster and not matched with TOF in the single TOF vertex with two TOF-matched tracks, an event is rejected. Such configuration implies higher-

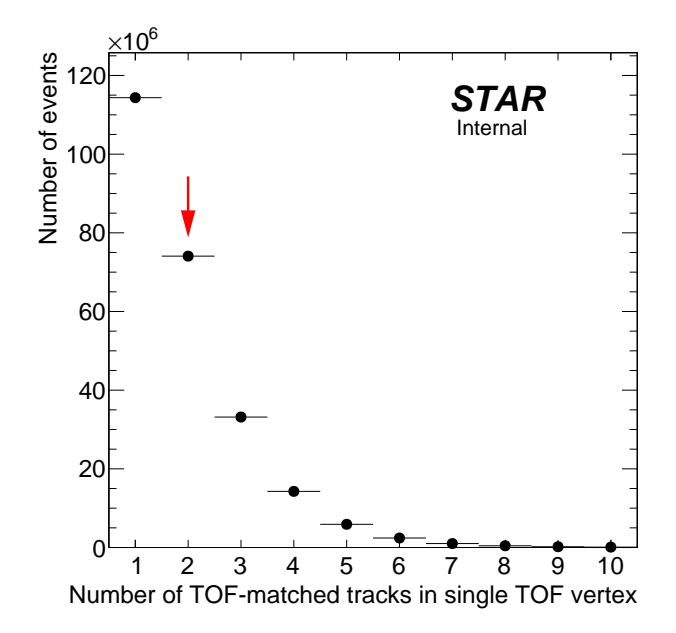
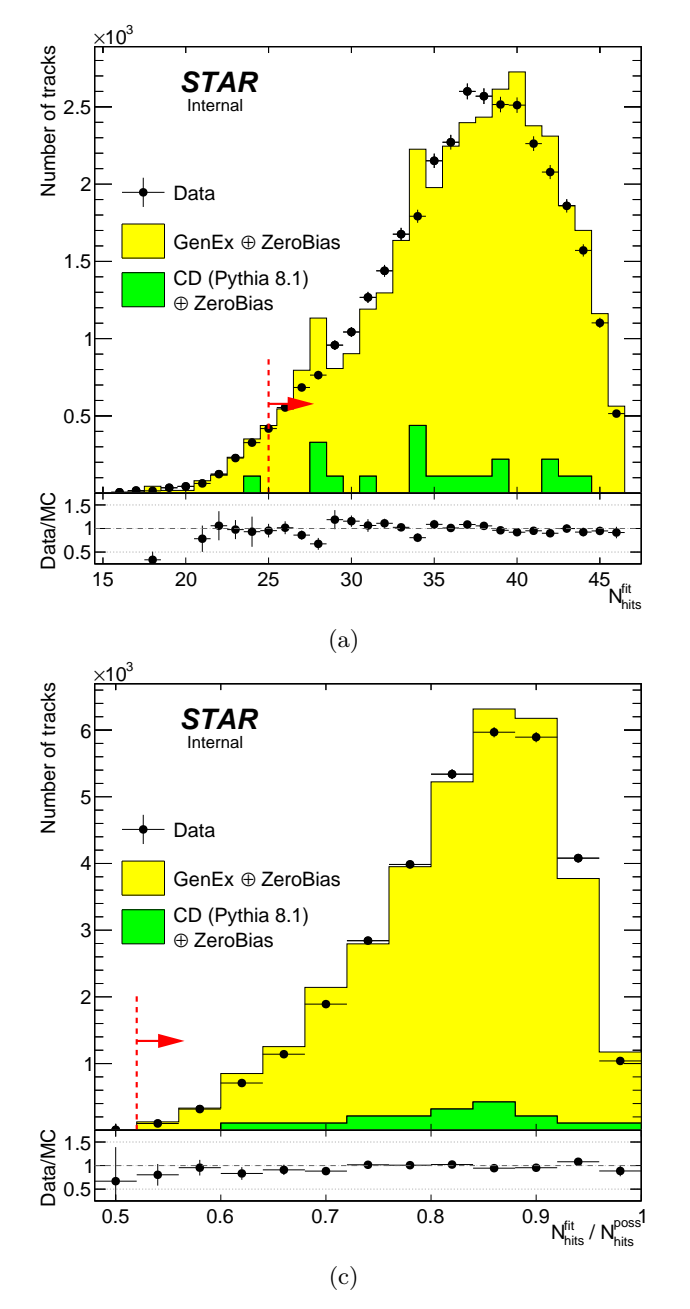


Figure 3.3: Multiplicty of primary TPC tracks matched with hit in TOF for single TOF vertex events. Red arrow marks bin with events with exactly two primary tracks matched with hit in TOF, which are used in physics analysis.

Figure 3.4: Distribution of a distance in $\eta-\phi$ space between the BEMC cluster closest to primary TPC track matched (filled circle) or not matched (opened circle) with hit in TOF, for single TOF vertex events. Red dashed line indicate matching threshold $R_{\rm max}^{\rm match}=0.05$.

than-2 multiplicty of the real tracks in the vertex, hence an event is unlikely a Central Exclusive Production of two particles.



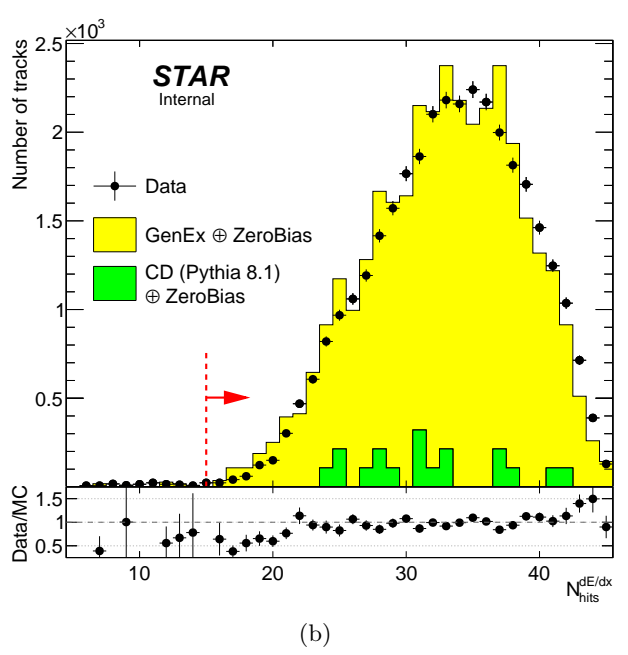


Figure 3.5: Comparison of distribution of the number of hits used in TPC track reconstrucion $N_{\rm hits}^{\rm fit}$ (3.5a), number of hits used in specific energy loss reconstrucion $N_{\rm hits}^{\rm dE/dx}$ (3.5b) and fraction of number of hits potentially generated by the track and finally used in the reconstrucion $N_{\rm hits}^{\rm fit}/N_{\rm hits}^{\rm poss}$ (3.5c) in the data and embedded MC. Normalizations of the signal and backgrounds were established from the comparison of $p_T^{\rm miss}$ and $\Delta\theta$ distributions after full selection (without cut on the presented quantity and without exclusivity cut), as described in Sec. 5.2. Red dashed line and red arrow indicate the range of each quantity which is accepted in analysis.

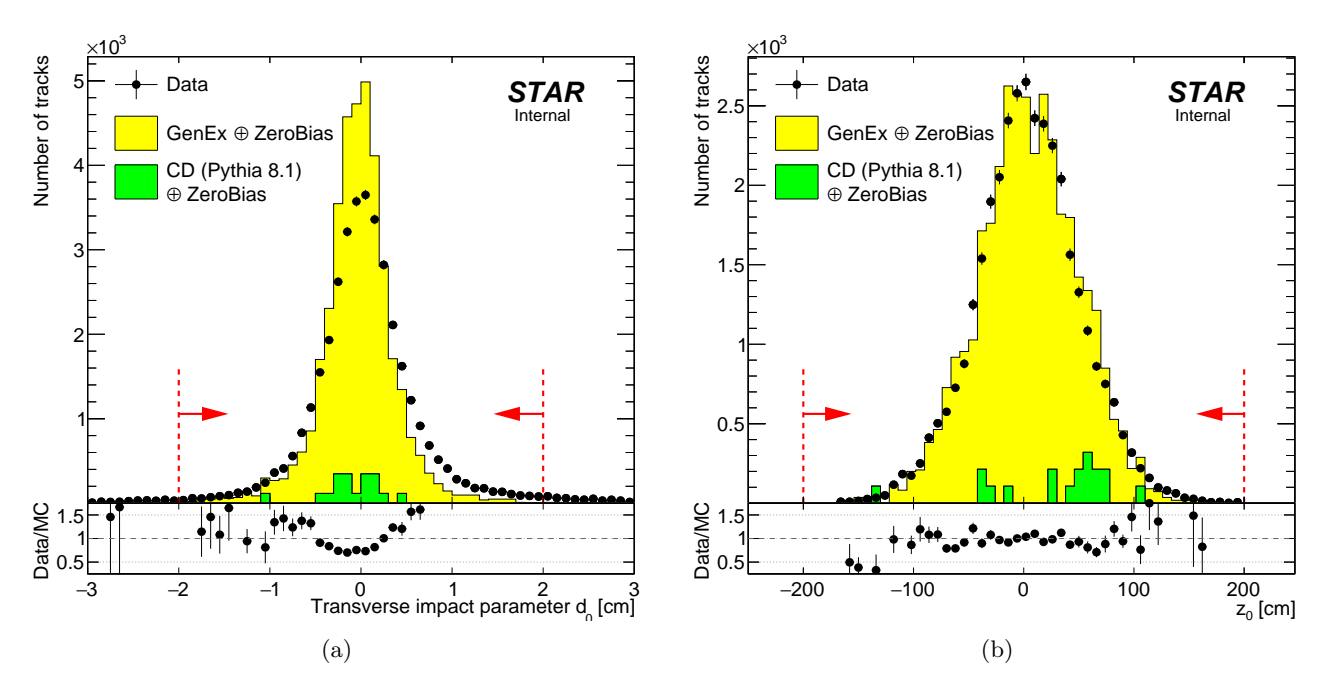


Figure 3.6: Comparison of distribution of the transverse impact parameter d_0 (3.6a) and the longitudinal impact parameter z_0 (3.6b) in the data and embedded MC. Normalizations of the signal and backgrounds were established from the comparison of p_T^{miss} and $\Delta\theta$ distributions after full selection (without cut on the presented quantity and without exclusivity cut), as described in Sec. 5.2. Red dashed lines and red arrows indicate the range of each quantity which is accepted in analysis.

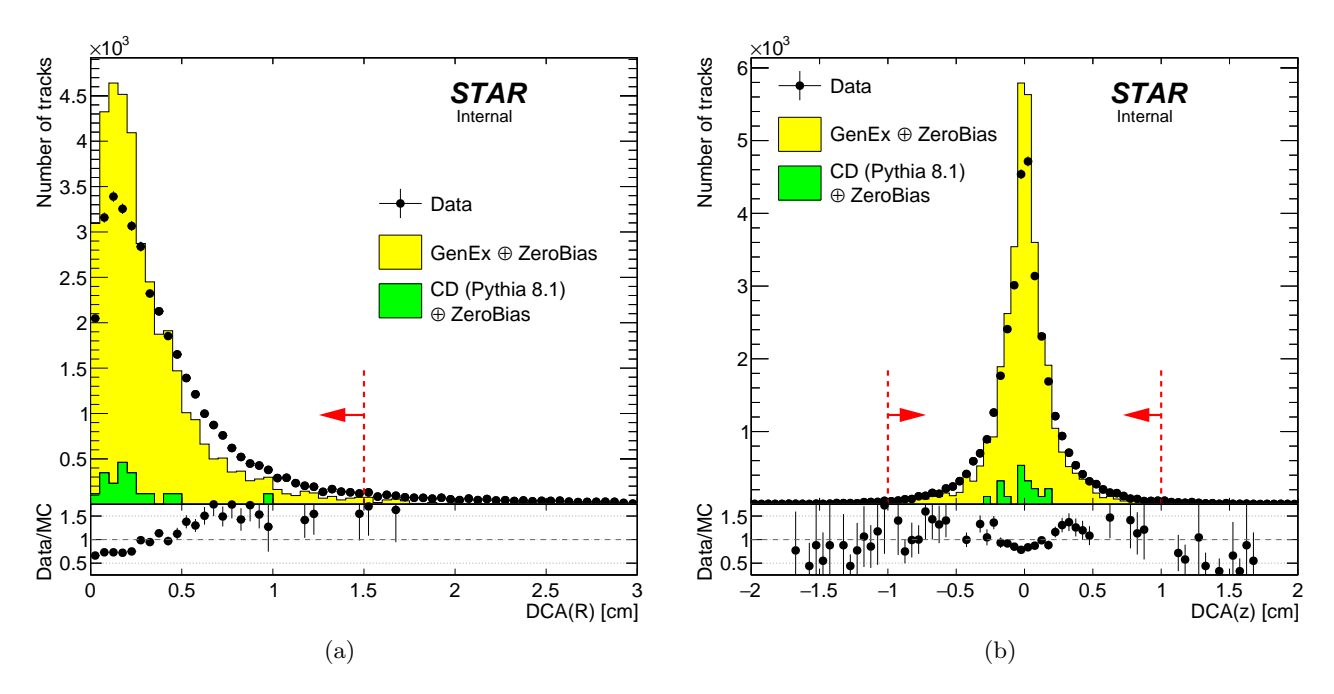


Figure 3.7: Comparison of distribution of the distance of closest approach of the track to the vertex in the xy-plane DCA(R) (3.7a) and the distance of closest approach of the track to the vertex along the z-axis DCA(z) (3.7b) in the data and embedded MC. Normalizations of the signal and backgrounds were established from the comparison of $p_T^{\rm miss}$ and $\Delta\theta$ distributions after full selection (without cut on the presented quantity and without exclusivity cut), as described in Sec. 5.2. Red dashed lines and red arrows indicate the range of each quantity which is accepted in analysis.

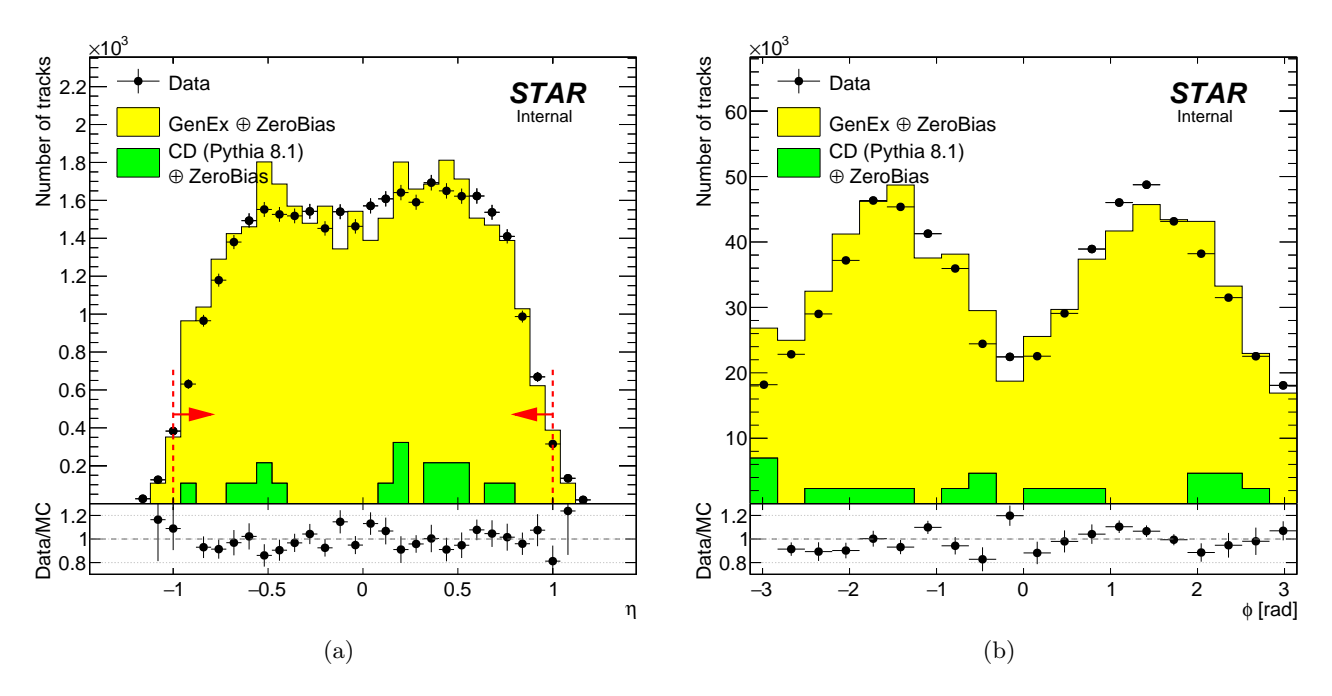


Figure 3.8: Comparison of the track pseudorapidity η (3.8a) and the track azimuthal angle ϕ (3.8b) in the data and embedded MC. Normalizations of the signal and backgrounds were established from the comparison of $p_T^{\rm miss}$ and $\Delta\theta$ distributions after full selection (without cut on the presented quantity and without exclusivity cut), as described in Sec. 5.2. Red dashed lines and red arrows indicate the range of each quantity which is accepted in analysis.

3.2.3 (C4) RP tracks

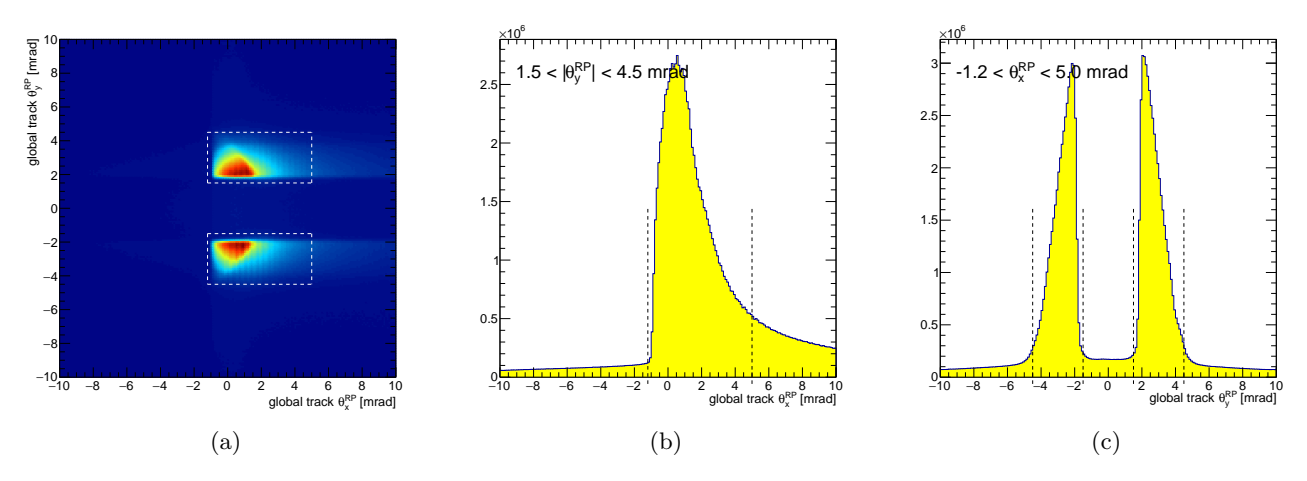


Figure 3.9: Local angles of global tracks in Roman Pots.

3.2.4 (C5) TPC-RP z-vertex matching

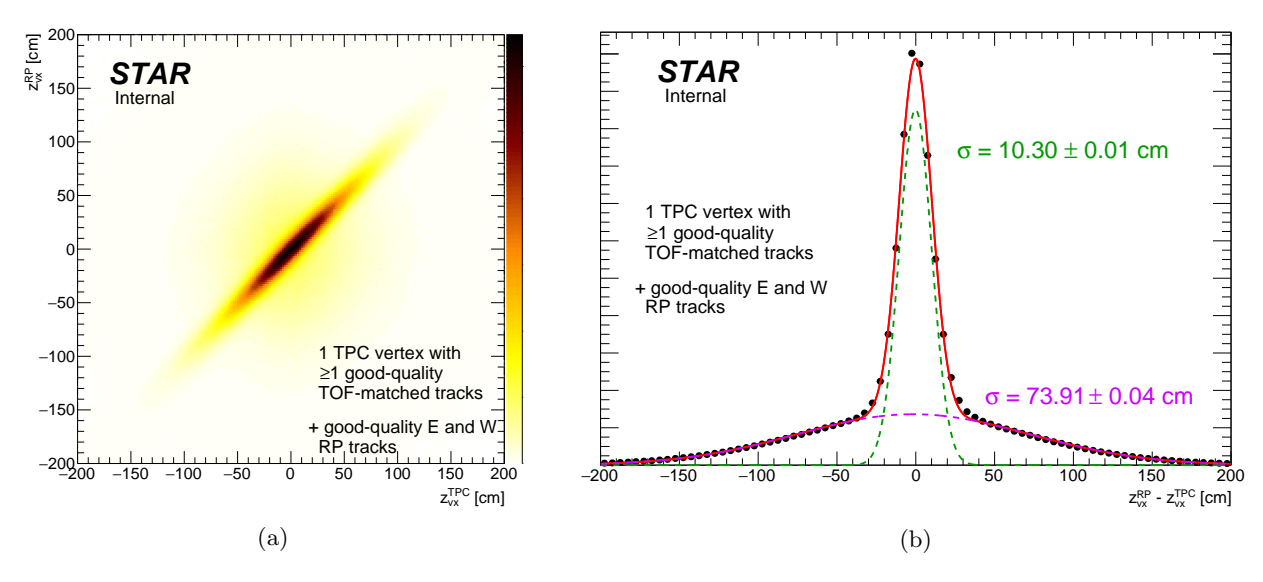


Figure 3.10: Correlation (Fig. 3.10a) and difference (Fig. 3.10b) of z-vertex position measured in Roman Pots and TPC.

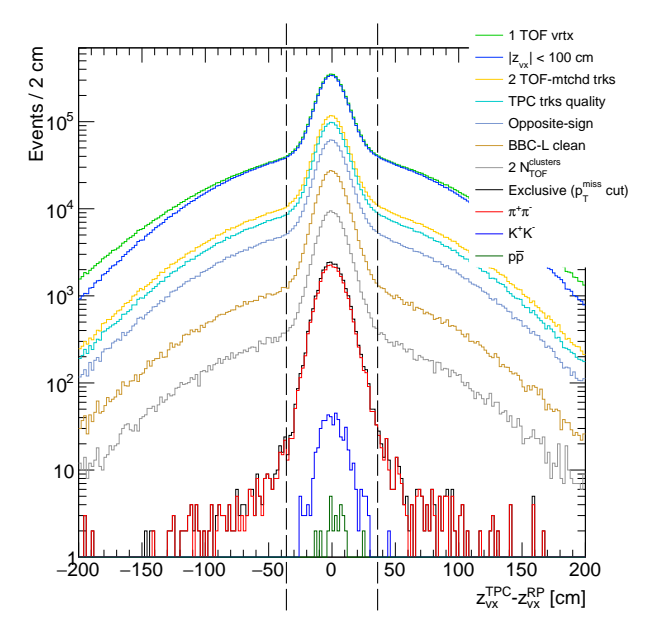


Figure 3.11: Delta z-vx.

3.2.5 (C6) BBC-large signal veto

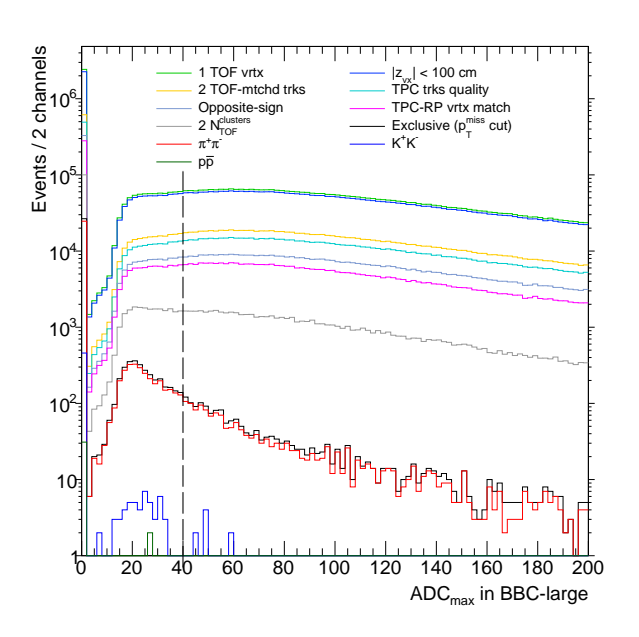


Figure 3.12: MaxAdcBbcLarge.

3.2.6 (C7) TOF clusters limit

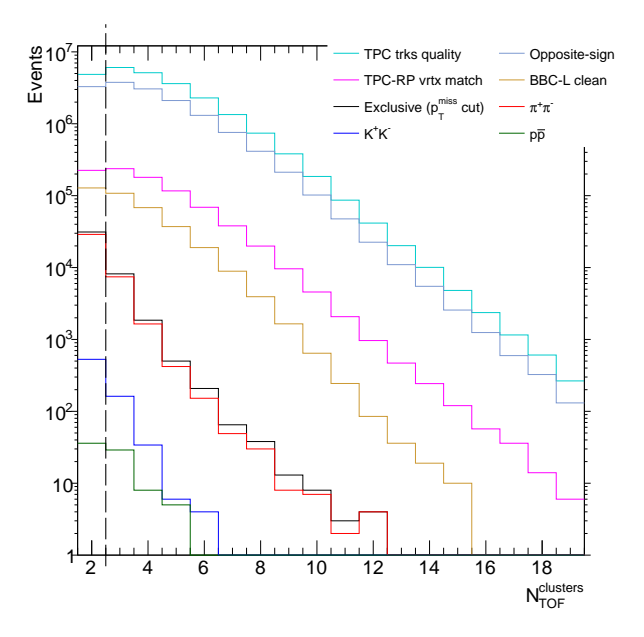


Figure 3.13: NTofClusters.

3.2.7 (C8) Exclusivity cut (missing p_T cut)

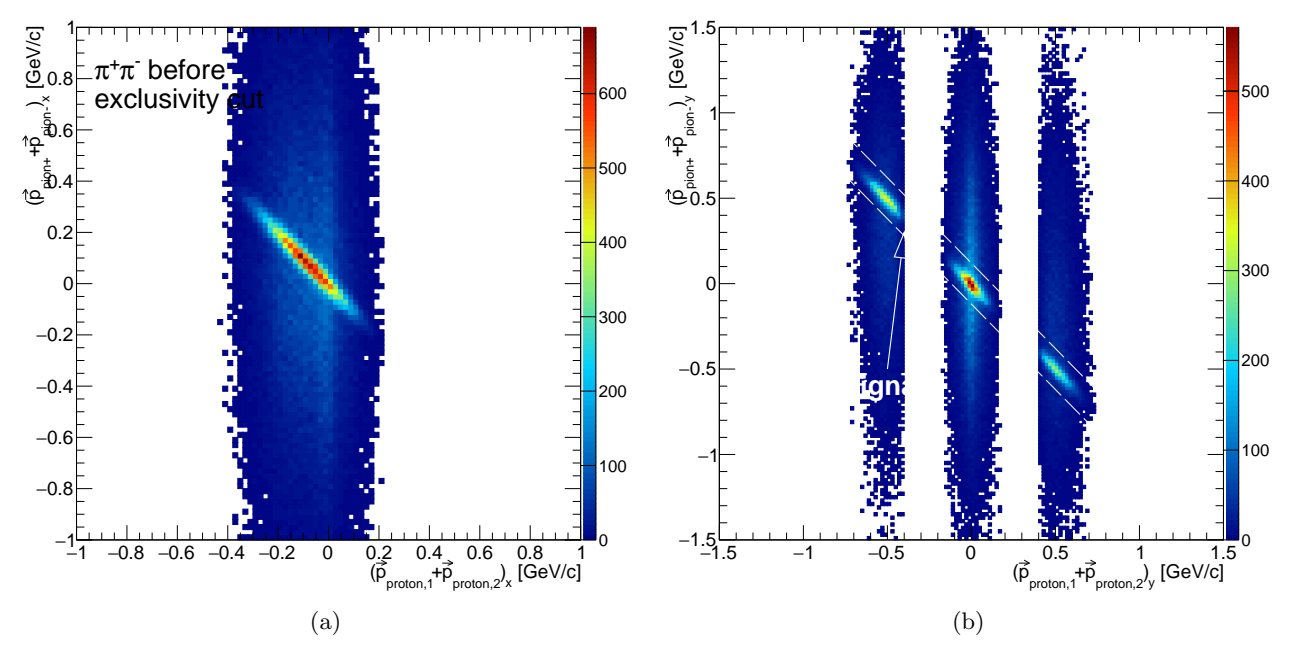


Figure 3.14: Correlation between sum of corresponding momentum components (x in Fig. 3.14a and y in Fig. 3.14b) of Roman Pot proton tracks and TPC tracks.

Tutaj dodac rysunki z suma 1D tych wielkosci i uzasadnic stosowanie ciecia na missing pT takimi samymi rozdzielczosciami wxi y

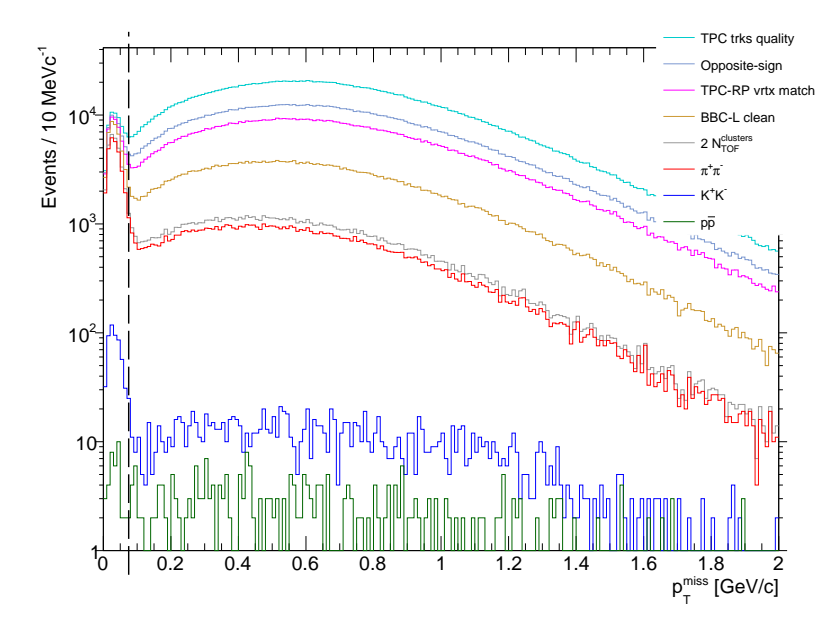


Figure 3.15: MissingPt.

3.2.8 (C9) Particle identification

In addition to information from the TPC we use time of hit detection in the barrel TOF subsystem. From the simple algebra describing relation between track lengths, momenta and times of hit detection one can derive formula for the squared mass of two particles, assuming that their masses are equal (particles are of the same type):

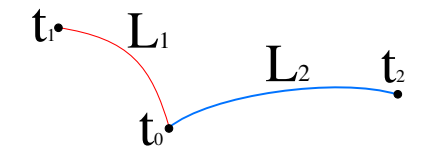


Figure 3.16: Scheme of two central tracks of lengths L_1 and L_2 , produced in common vertex in moment t_0 , hitting cells in TOF detector in moments t_1 and t_2 .

$$\begin{cases}
t_1 - t_0 = L_1 \sqrt{1 + \frac{m_1^2}{p_1^2}}, \\
t_2 - t_0 = L_2 \sqrt{1 + \frac{m_2^2}{p_2^2}},
\end{cases}$$
(3.2)

$$\Delta t = t_1 - t_2 = L_1 \sqrt{1 + \frac{m_1^2}{p_1^2}} - L_2 \sqrt{1 + \frac{m_2^2}{p_2^2}}.$$
(3.3)

Assuming $m_1 = m_2 = m \rightarrow m^2$ from quadratic eq.

Parameters of the quadratic equation whose solution is suqared mass and the final formula for m_{TOF}^2 are given below:

$$\mathcal{A} = -2\frac{L_1^2 L_2^2}{p_1^2 p_2^2} + \frac{L_1^4}{p_1^4} + \frac{L_2^4}{p_2^4},\tag{3.4}$$

$$\mathcal{B} = -2L_1^2 L_2^2 \left(\frac{1}{p_1^2} + \frac{1}{p_2^2} \right) + \frac{2L_1^4}{p_1^2} + \frac{2L_2^4}{p_2^2} - 2\left(\Delta t\right)^2 \left(\frac{L_1^2}{p_1^2} + \frac{L_2^2}{p_2^2} \right),\tag{3.5}$$

$$C = (\Delta t)^4 - 2(\Delta t)^2 (L_1^2 + L_2^2) + L_1^4 + L_2^4 - 2L_1^2 L_2^2,$$
(3.6)

$$m_{\text{\tiny TOF}}^2 = \frac{-\mathcal{B} + \sqrt{\mathcal{B}^2 - 4\mathcal{AC}}}{2\mathcal{A}}.$$
 (3.7)

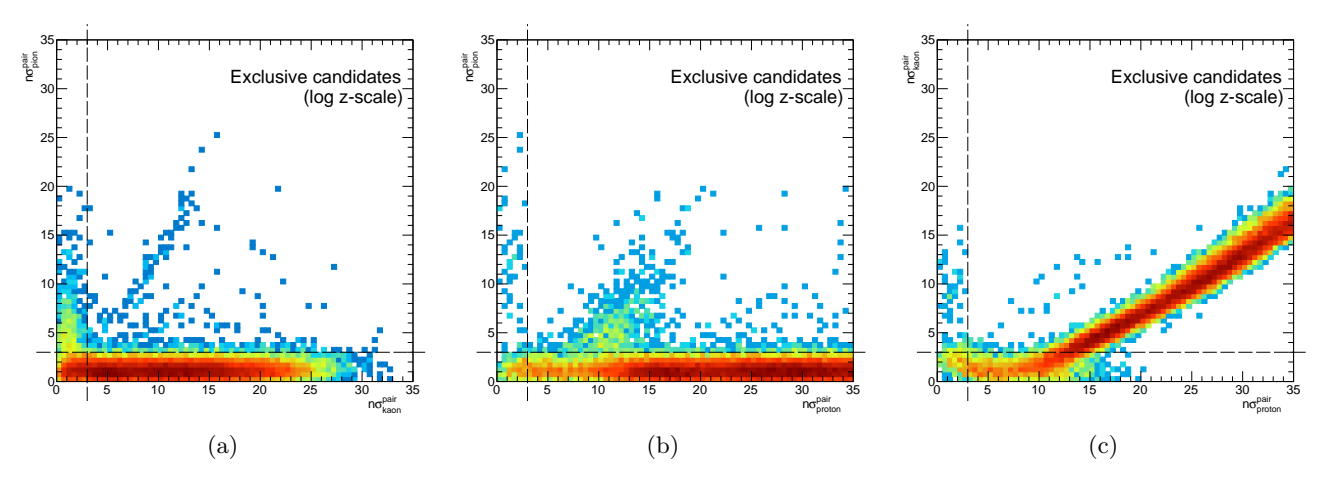


Figure 3.17: Correlation between $n\sigma^{\text{pair}}$ from TPC for $\pi^+\pi^-$, K^+K^- and $p\bar{p}$.

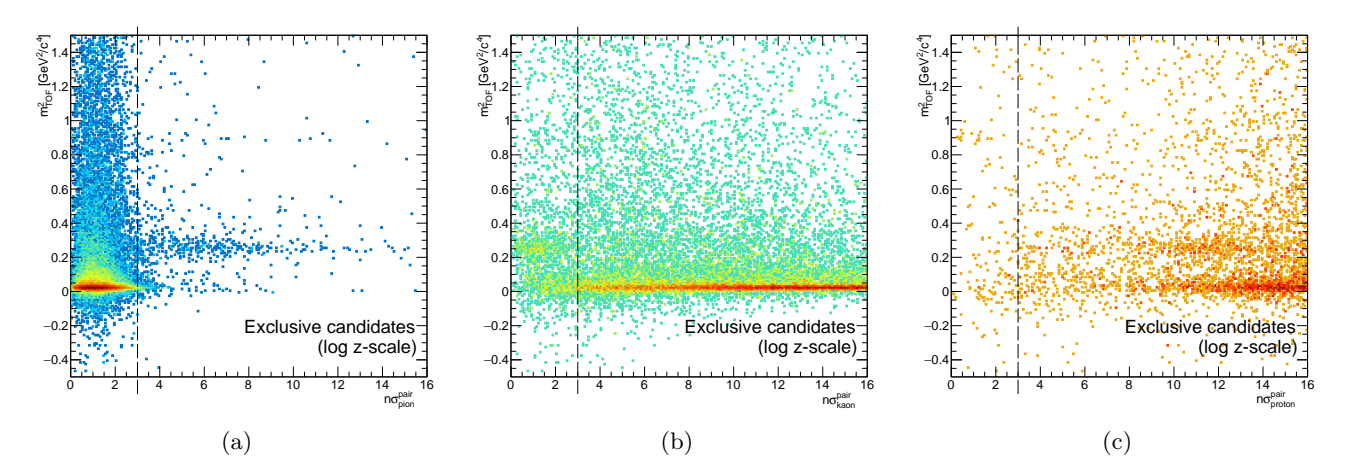


Figure 3.18: Correlation between m^2 from TOF and $n\sigma^{\text{pair}}$ from TPC for $\pi^+\pi^-$, K^+K^- and $p\bar{p}$.

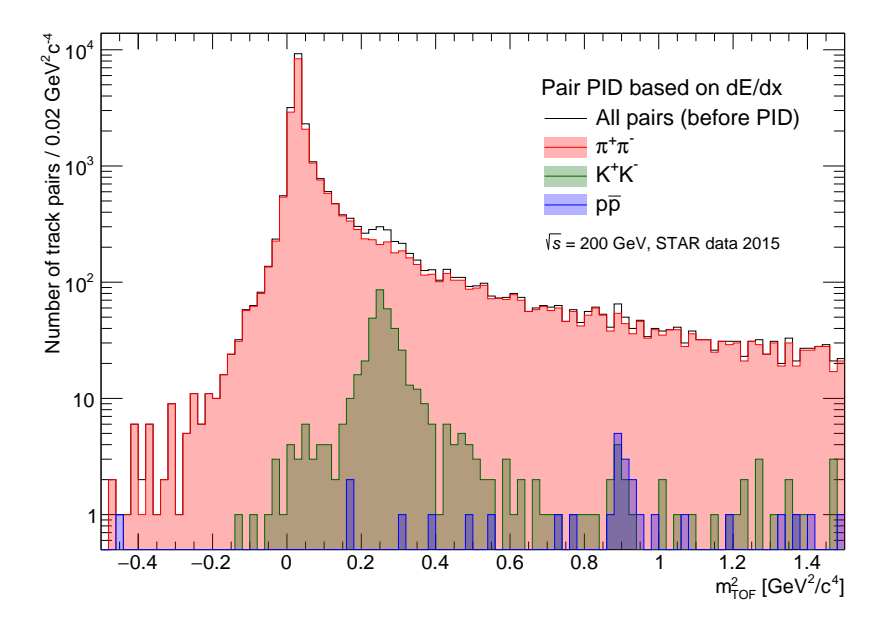
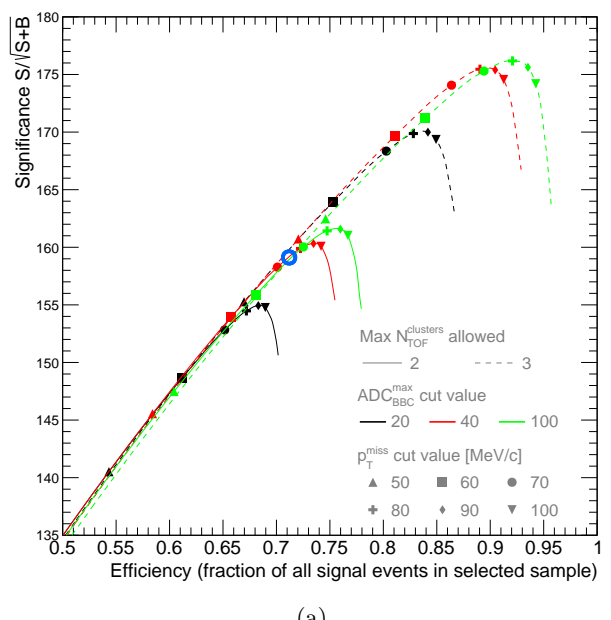
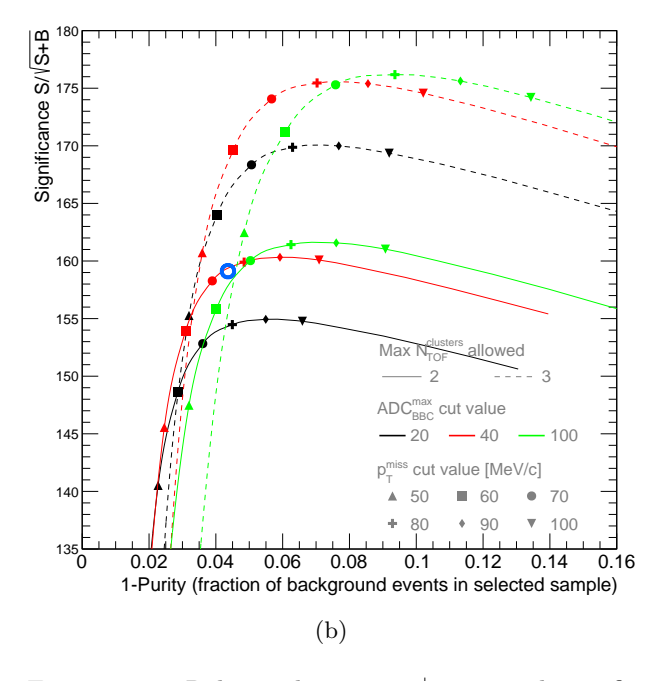


Figure 3.19: Squared particle mass from TOF for candidates of given PID selected based on dE/dx in TPC.

3.3 Working point for cuts C6, C7 and C8

$$\text{Significance} = \frac{N_{\text{signal}}^{\text{cut}}}{\sqrt{N_{\text{signal}}^{\text{cut}} + N_{\text{bkgd}}^{\text{cut}}}}, \quad (3.8) \quad \text{Efficiency} = \frac{N_{\text{signal}}^{\text{cut}}}{N_{\text{signal}}^{\text{no cut}}}, \quad (3.9) \quad \text{Purity} = \frac{N_{\text{signal}}^{\text{cut}}}{N_{\text{signal}}^{\text{cut}} + N_{\text{bkgd}}^{\text{cut}}}, \quad (3.10)$$





29mble) 95 e constant selected s 0.85 0.8 all signal e ਰੂੰ 0.7 allowed (fragion 59:62 cut value Efficiency (cut value [MeV/c] 100 0.12 0.06 0.08 0.1 0.14 1-Purity (fraction of background events in selected sample) (c)

Figure 3.20: Relation between $\pi^+\pi^-$ signal significance and efficiency (3.20a), significance and purity (3.20b), and efficiency and purity (3.20c) as a function of cut thresholds in BBC-large veto (C6), TOF cluster limit (C7) and exclusivity cut (C8). Lines show forementioned relations with changing p_T^{miss} cut whose some specific values are indicated with different markers. Color denotes ADC threshold in BBC-large veto (black, red or green). Style of line (solid or dashed) denotes $N_{\text{clstrs}}^{\text{TOF}}$ limit. Working point considered optimal is marked with opened blue circle.

3.4 Signal per integrated luminosity

3.5 Cut flow

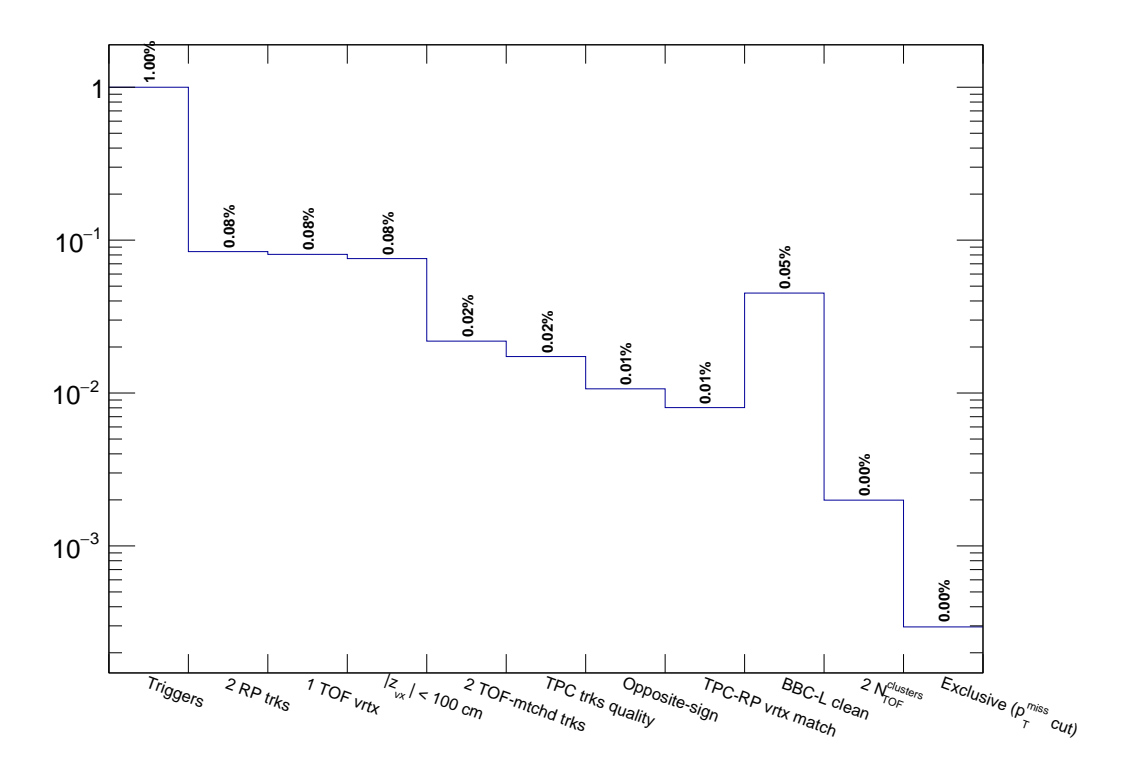


Figure 3.21: Cut flow.

4. Corrections

4.1 Method of corrections application

$$\frac{d\sigma}{dq} = \frac{1}{\Delta q} \times \frac{1}{\varepsilon} \times \frac{N^w - N_{\text{bkgd}}^w}{L_{\text{int}}^{\text{eff}}}$$
(4.1)

$$L_{\rm int}^{\rm eff} = \sum_{\rm run} L_{\rm int}^{\rm run} \times \epsilon_{\rm veto}(L^{\rm run})$$
(4.2)

$$\varepsilon = \epsilon_{\text{ET/IT}} \times \epsilon_{\text{vrtx}}(q) \times \epsilon_{C2} \times \epsilon_{C5} \times \epsilon_{C8} \times \epsilon_{\text{PID}}(q)$$
(4.3)

$$N^w = \sum_{\text{event}} w_{\text{event}} \tag{4.4}$$

$$w = \left[\prod_{\text{sign}} \epsilon_{\text{TOF}}(\text{sign}, \text{PID}, p_T, z_{vx}, \eta) \times \prod_{\text{sign}} \epsilon_{\text{TPC}}(\text{sign}, \text{PID}, p_T, z_{vx}, \eta) \times \prod_{\text{side}} \epsilon_{\text{RP}}^{\text{side}}(p_x, p_y) \right]^{-1},$$

$$\text{sign} \in \{+, -\}, \text{ side} \in \{E, W\}$$

$$(4.5)$$

4.2 Efficiencies and acceptances

In this section we present calculation of all efficiencies except TPC track reconstruction and TOF hit reconstruction and matching efficiency, which were discussed and presented in Ref. [1].

4.2.1 Trigger efficiency

4.2.1.1 Online veto (BBC-small and ZDC veto)

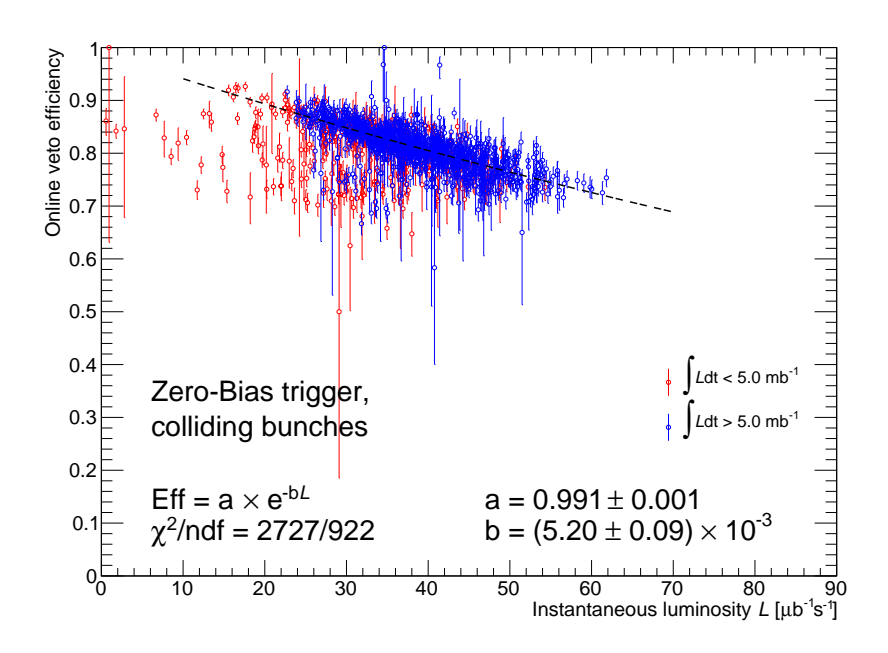


Figure 4.1: Overall efficiency of the online BBC-small and ZDC veto as a function of instantaneous luminosity.

- 4.2.1.2 RP triggering efficiency
- 4.2.1.3 Up and Down RP combination veto
- 4.2.2 Cuts efficiency
- 4.2.2.1 TPC z-vertex cut (C2)
- 4.2.2.2 TPC-RP z-vertex matching (C5)
- 4.2.2.3 Primary vertices limit (C1), BBC-large veto (C6) and TOF clusters limit (C7)

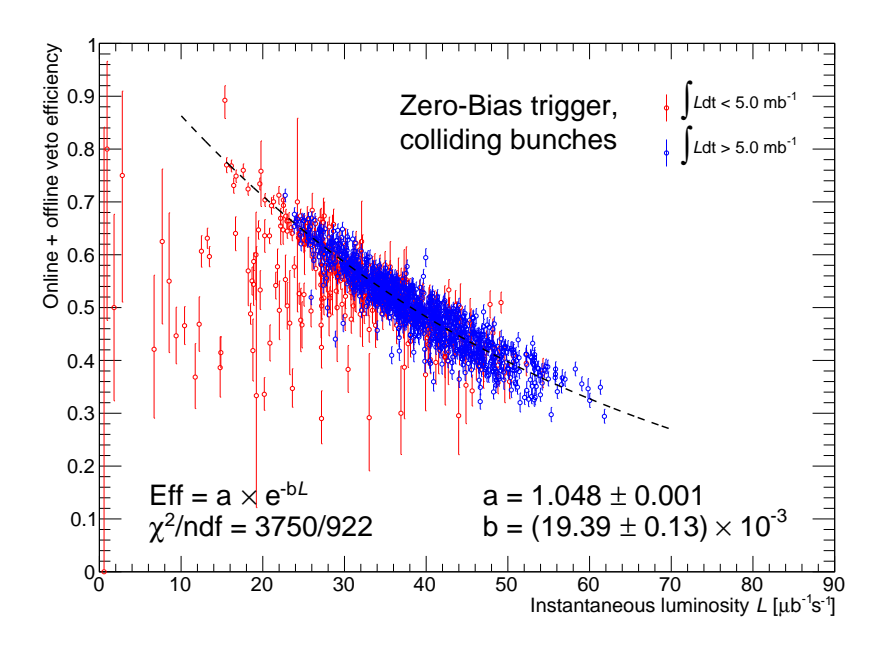


Figure 4.2: Overall efficiency of the online BBC-small and ZDC veto, primary vertices limit (C1), BBC-large veto (C6) and TOF clusters limit (C7) as a function of instantaneous luminosity.

4.2.2.4 Missing p_T cut (C8)

4.2.2.5 Particle identification (C9)

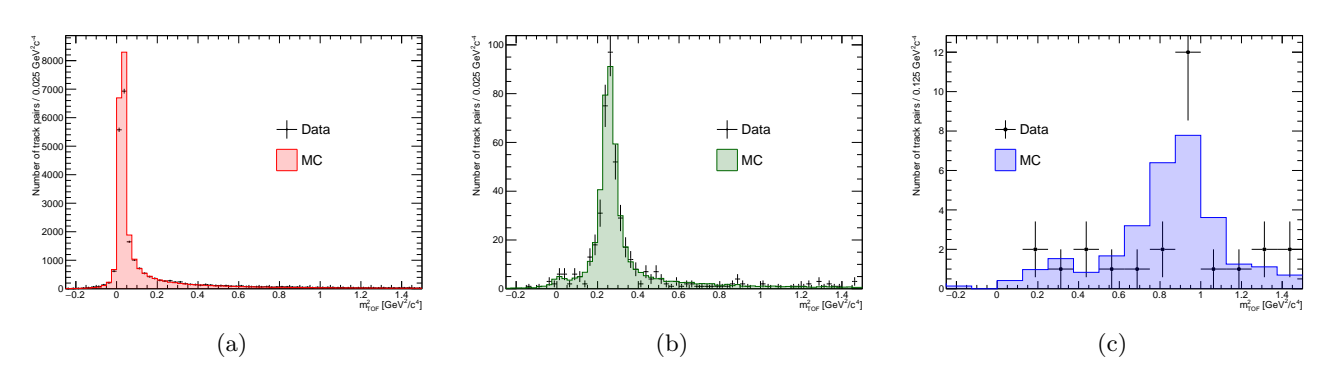


Figure 4.3: Comparison of m^2 from TOF between data and MC for exclusive $\pi^+\pi^-$, K^+K^- and $p\bar{p}$.

4.2.3 RP track acceptance and reconstruction efficiency

4.2.4 TPC vertex reconstruction efficiency

The definition of vertex reconstruction efficiency established in this analysis is the probability that two global tracks, both associated with true-level primary particles from the kinematic region of the measurement, both satisfying kinematic and quality criteria (cuts C3.3 and C3.4) and both matched with hits in TOF, form a

vertex listed in the collection of reconstructed primary vertices and DCA(R) and DCA(z) of both global tracks calculated w.r.t. this vertex is contained within the limits of cut C3.5.

- 4.3 Particle energy loss
- 4.4 Background subtraction
- 4.5 Unfolding

5. Backgrounds

5.1 Sources of background

5.1.1 Non-exclusive background

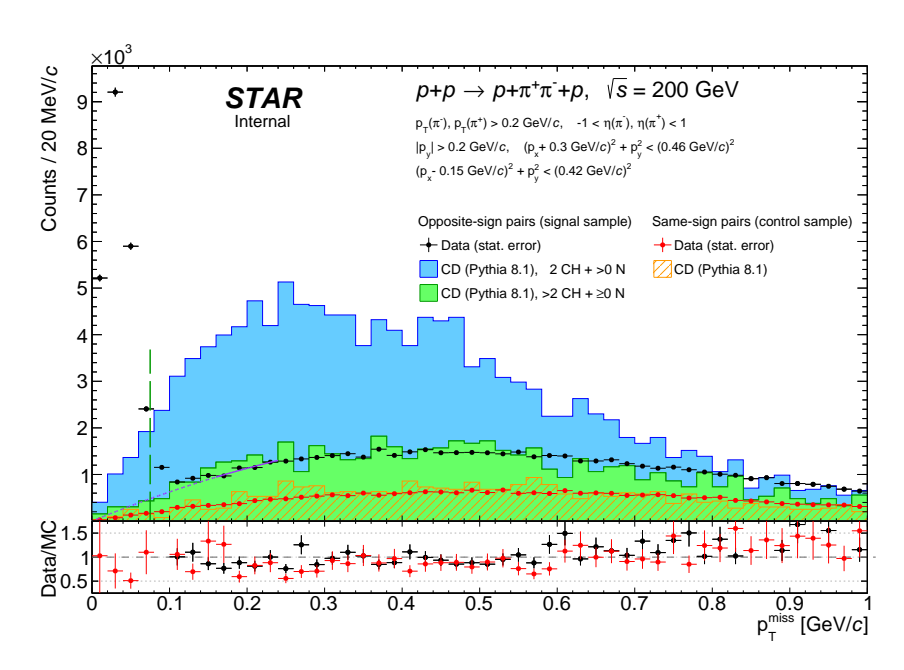


Figure 5.1: Missing pT.

tutaj dodac szkice spodziewanego tla nieekskluzywnego

5.1.2 Exclusive background (particle misidentification)

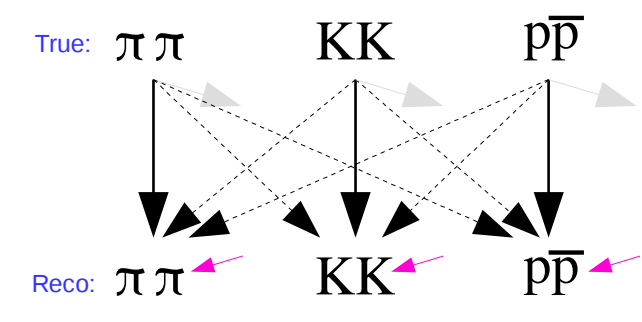


Figure 5.2: Graph illustrating the misidentification problem - the origin of exclusive background in selected samples. Gray arrows represent event rejection due to failed PID selection (C9). Magenta arrows indicate non-exclusive backgrounds described in Sec. 5.1.1. Solid black arrows represent successful identification, whereas dashed black lines show misidentification paths.

$$N_{R}^{\pi\pi} = \underbrace{\epsilon^{\pi\pi} \cdot N_{T}^{\pi\pi}}_{\text{true pion pairs}} + \underbrace{\lambda^{KK \to \pi\pi} \cdot N_{T}^{KK}}_{\text{kaon pairs reconstructed as pion pairs}}_{\text{kaon pairs}} + \underbrace{\lambda^{p\bar{p} \to \pi\pi} \cdot N_{T}^{p\bar{p}}}_{\text{proton pairs reconstructed as pion pairs}} + \underbrace{N_{bkgd}^{\pi\pi}}_{\text{bkgd}}$$
(5.1a)
$$N_{R}^{KK} = \underbrace{\lambda^{\pi\pi \to KK} \cdot N_{T}^{\pi\pi}}_{\text{pion pairs reconstructed as kaon pairs}} + \underbrace{\epsilon^{KK} \cdot N_{T}^{KK}}_{\text{true kaon pairs}} + \underbrace{\lambda^{p\bar{p} \to KK} \cdot N_{T}^{p\bar{p}}}_{\text{proton pairs reconstructed as kaon pairs}} + \underbrace{N_{bkgd}^{KK}}_{\text{bkgd}}$$
(5.1b)
$$N_{R}^{p\bar{p}} = \underbrace{\lambda^{\pi\pi \to p\bar{p}} \cdot N_{T}^{\pi\pi}}_{\text{pion pairs reconstructed}} + \underbrace{\lambda^{KK \to p\bar{p}} \cdot N_{T}^{KK}}_{\text{kaon pairs reconstructed}} + \underbrace{\lambda^{p\bar{p} \to KK} \cdot N_{T}^{p\bar{p}}}_{\text{true proton pairs}} + \underbrace{N_{bkgd}^{p\bar{p}}}_{\text{bkgd}}$$
(5.1c)

Eqs. (5.1) can be written in the matrix form, as shown in Eq. (5.2), from which it is straightforward to obtain final formula for unfolded number of events of given ID, Eq. (5.3):

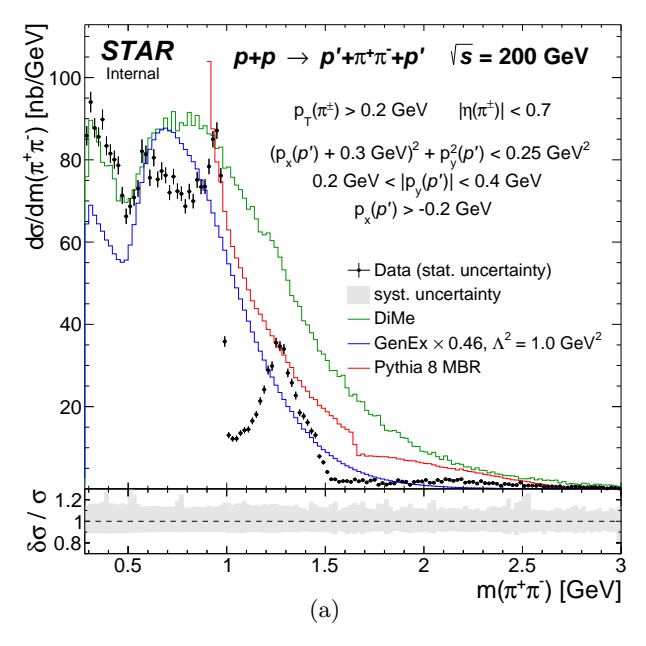
$$\begin{bmatrix} N_{R}^{\pi\pi} - N_{bkgd}^{\pi\pi} \\ N_{R}^{KK} - N_{bkgd}^{KK} \\ N_{R}^{p\bar{p}} - N_{bkgd}^{p\bar{p}} \end{bmatrix} = \underbrace{\begin{bmatrix} \epsilon^{\pi\pi} & \lambda^{KK \to \pi\pi} & \lambda^{p\bar{p} \to \pi\pi} \\ \lambda^{\pi\pi \to KK} & \epsilon^{KK} & \lambda^{p\bar{p} \to KK} \\ \lambda^{\pi\pi \to p\bar{p}} & \lambda^{KK \to p\bar{p}} & \epsilon^{p\bar{p}} \end{bmatrix}}_{\text{"mixing matrix" } \Lambda} \begin{bmatrix} N_{T}^{\pi\pi} \\ N_{T}^{KK} \\ N_{T}^{p\bar{p}} \end{bmatrix} \rightarrow \begin{bmatrix} N_{T}^{\pi\pi} \\ N_{T}^{KK} \\ N_{T}^{p\bar{p}} \end{bmatrix} = \Lambda^{-1} \begin{bmatrix} N_{R}^{\pi\pi} - N_{bkgd}^{\pi\pi} \\ N_{R}^{KK} - N_{bkgd}^{KK} \\ N_{R}^{p\bar{p}} - N_{bkgd}^{p\bar{p}} \end{bmatrix}$$

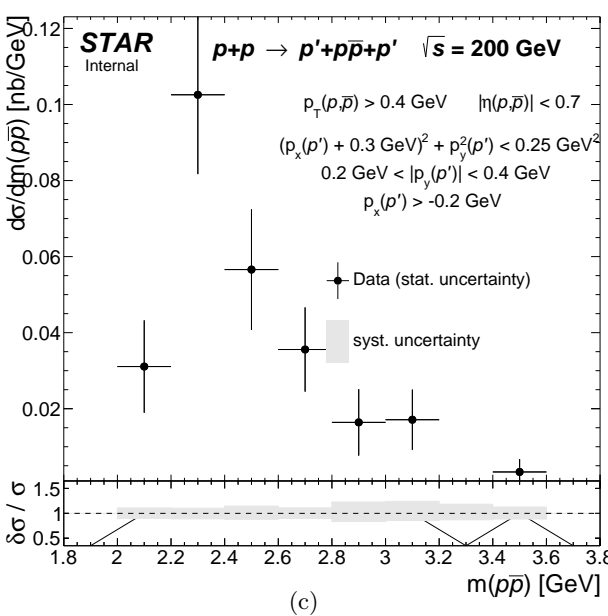
$$(5.2)$$

5.2 Relative normalization of background and signal

6. Systematic errors

7. Physics results





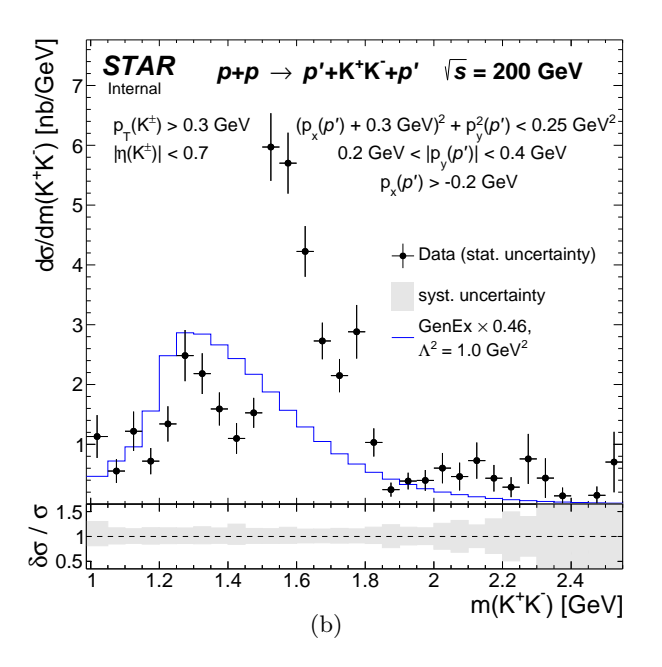
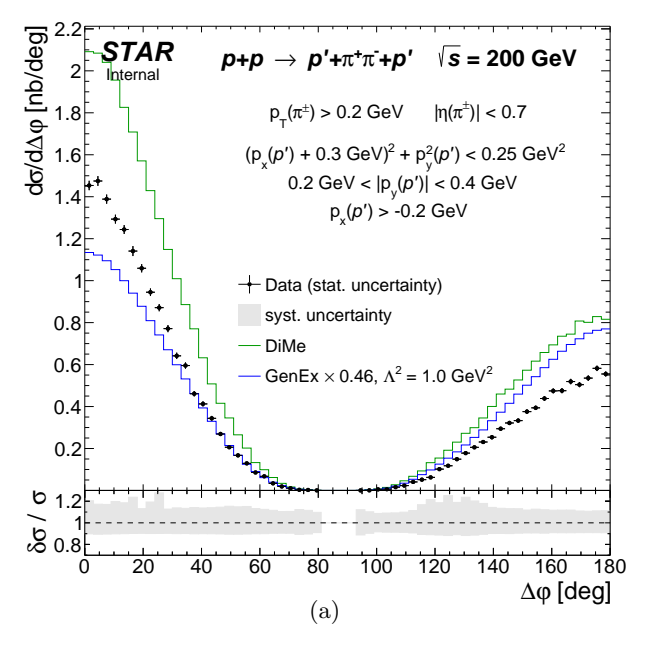
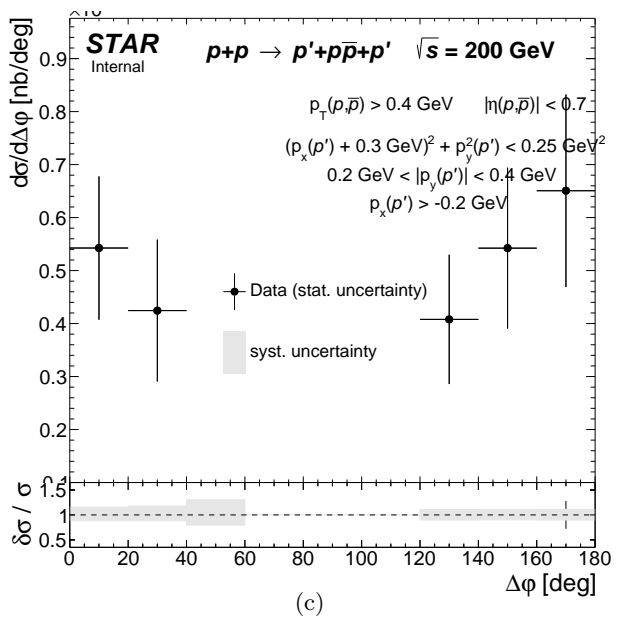


Figure 7.1





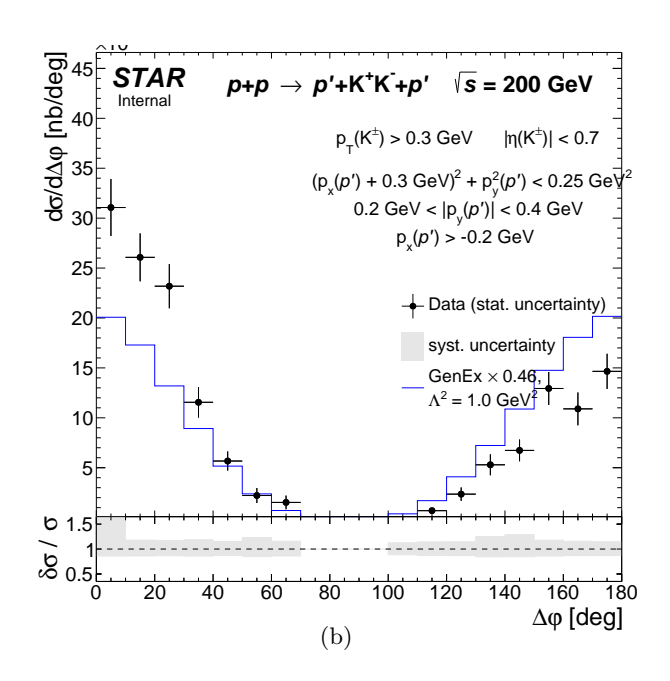
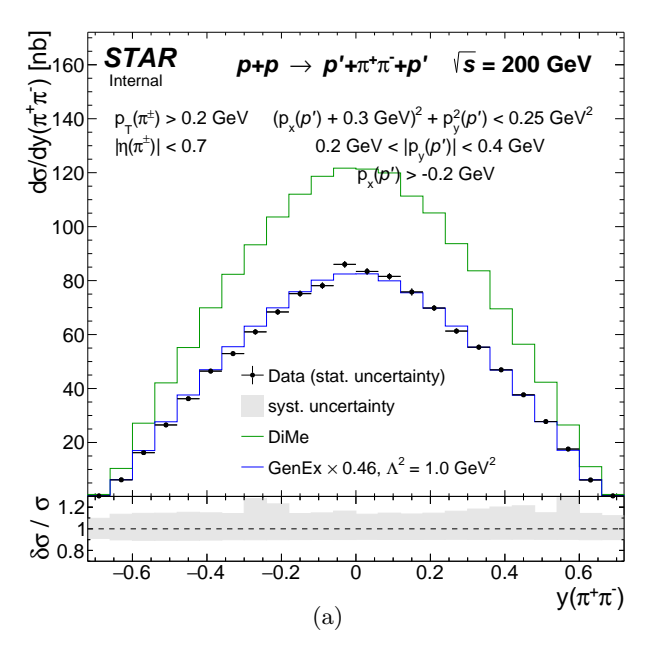
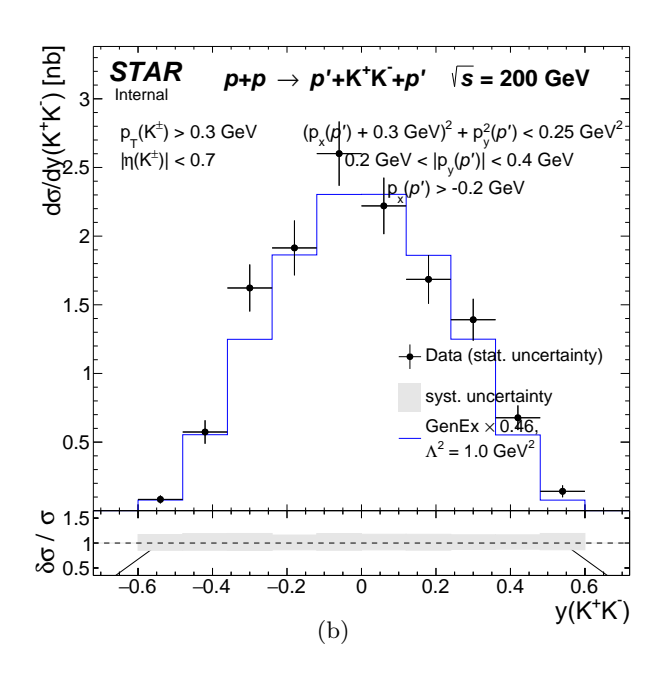


Figure 7.2





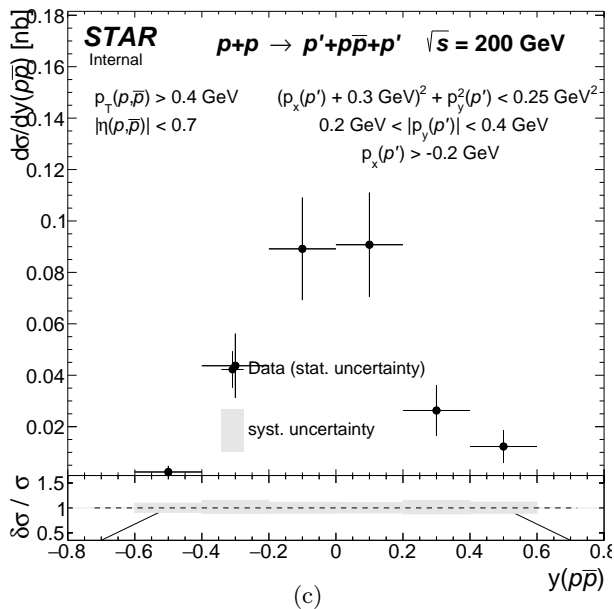


Figure 7.3

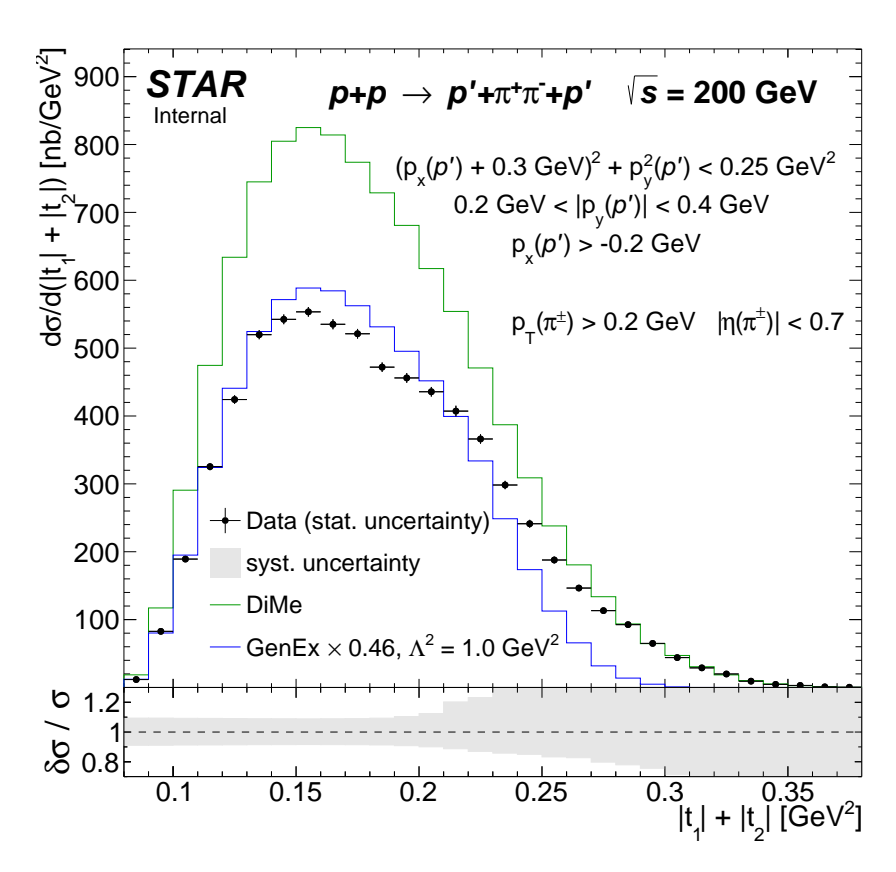


Figure 7.4: Cut flow.

List of Figures

$1.1 \\ 1.2$	CEP represented in η - ϕ space	5 5
2.1	Sketch of the trigger components used in definitions of diffractive triggers in run 15	7
3.1	Primary vertex multiplicty. Red arrow marks bin with events with exactly one primary vertex (with track(s) matched with hit in TOF), which are used in physics analysis. 10	
3.2	z-position of the primary vertex in single TOF vertex events. Red dashed line indicate range of longitudinal vertex position accepted in analysis	10
3.3 3.4	Multiplicity of primary TPC tracks matched with hit in TOF for single TOF vertex events Distribution of a distance in $\eta - \phi$ space between the BEMC cluster closest to primary TPC track	11
-	(R_{\min})	11
3.5	Comparison of distribution of $N_{\rm hits}^{\rm fit}$, $N_{\rm hits}^{\rm dE/dx}$ and $N_{\rm hits}^{\rm fit}/N_{\rm hits}^{\rm poss}$ in the data and embedded MC	12
3.6	Comparison of distribution of d_0 and z_0 in the data and embedded MC	13
3.7	Comparison of distribution of $DCA(R)$ and $DCA(z)$ in the data and embedded MC	13
3.8	Comparison of distribution of track η and ϕ in the data and embedded MC	14
3.9	Local angles of global tracks in Roman Pots.	15
	Correlation and difference of z-vertex position measured in Roman Pots and TPC	15
	Delta z-vx.	16
	MaxAdcBbcLarge	16
	NTofClusters	17
	Fig. 3.14b) of Roman Pot proton tracks and TPC tracks	17
	MissingPt	18
	Scheme of two central tracks with common vertex, hitting cells in TOF detector	18
	Correlation between $n\sigma^{\text{pair}}$ from TPC for $\pi^+\pi^-$, K^+K^- and $p\bar{p}$	19 19
	Squared particle mass from TOF for candidates of given PID selected based on dE/dx in TPC.	19
	Relation between $\pi^+\pi^-$ significance, efficiency and purity vs. thresholds in cuts C6, C7 and C8.	20
	Cut flow	21
0.21		21
$4.1 \\ 4.2$	Overall efficiency of the online BBC-small and ZDC veto as a function of instantaneous luminosity. Overall efficiency of the online BBC-small and ZDC veto, primary vertices limit (C1), BBC-large	22
	veto (C6) and TOF clusters limit (C7) as a function of instantaneous luminosity	23
4.3	Comparison of m^2 from TOF between data and MC for exclusive $\pi^+\pi^-$, K^+K^- and $p\bar{p}$	23
5.1	Missing pT	25
5.2	Graph illustrating the misidentification problem	25
7.1		28
7.2		29
7.3		30

7.4	Cut flow.																																																		3	31
-----	-----------	--	--	--	--	--	--	--	--	--	--	--	--	--	--	--	--	--	--	--	--	--	--	--	--	--	--	--	--	--	--	--	--	--	--	--	--	--	--	--	--	--	--	--	--	--	--	--	--	--	---	----

List of Tables

2.1 Central Diffraction physics triggers and control triggers involving Roman Pot detectors in run 15. 7

References

- [1] L. Adamczyk, L. Fulek, and R. Sikora, "Supplementary note on diffractive analyses of 2015 proton-proton data." https://drupal.star.bnl.gov/STAR/blog/rafals/supplementary-note-diffractive-analyses-2015-proton-proton-data, January, 2019.
- P. D. B. Collins, An Introduction to Regge Theory and High-Energy Physics. Cambridge Monographs on Mathematical Physics. Cambridge Univ. Press, Cambridge, UK, 2009. http://www-spires.fnal.gov/spires/find/books/www?cl=QC793.3.R4C695.
- [3] S. Donnachie, H. G. Dosch, O. Nachtmann, and P. Landshoff, Pomeron physics and QCD, vol. 19. 2002.
- [4] V. Barone and E. Predazzi, *High-Energy Particle Diffraction*, vol. v.565 of *Texts and Monographs in Physics*. Springer-Verlag, Berlin Heidelberg, 2002. http://www-spires.fnal.gov/spires/find/books/www?cl=QC794.6.C6B37::2002.
- [5] P. Lebiedowicz and A. Szczurek, "Exclusive $pp \to pp\pi^+\pi^-$ reaction: From the threshold to LHC," *Phys. Rev.* **D81** (2010) 036003, arXiv:0912.0190 [hep-ph].
- [6] P. Lebiedowicz, O. Nachtmann, and A. Szczurek, "Central exclusive diffractive production of $\pi^+\pi^-$ continuum, scalar and tensor resonances in pp and $p\bar{p}$ scattering within tensor pomeron approach," *Phys. Rev.* **D93** no. 5, (2016) 054015, arXiv:1601.04537 [hep-ph].
- [7] L. A. Harland-Lang, V. A. Khoze, and M. G. Ryskin, "Modelling exclusive meson pair production at hadron colliders," Eur. Phys. J. C74 (2014) 2848, arXiv:1312.4553 [hep-ph].
- [8] R. Fiore, L. Jenkovszky, and R. Schicker, "Resonance production in Pomeron-Pomeron collisions at the LHC," Eur. Phys. J. C76 no. 1, (2016) 38, arXiv:1512.04977 [hep-ph].
- [9] F. E. Close and A. Kirk, "A Glueball q anti-q filter in central hadron production," *Phys. Lett.* **B397** (1997) 333–338, arXiv:hep-ph/9701222 [hep-ph].
- [10] https://online.star.bnl.gov/rp/pp200/.
- [11] https://online.star.bnl.gov/RunLogRun15/.
- [12] http://www.star.bnl.gov/protected/common/common2015/trigger2015/lumipp200GeV/.
- [13] I. Alekseev and J. H. Lee, "Trigger Definitions for RP phase-II* for Run15." https://drupal.star.bnl.gov/STAR/system/files/trigger_updated_run15_v2.doc, December, 2014.
- [14] I. Alekseev, "Trigger with Roman Pots Phase II*." https://drupal.star.bnl.gov/STAR/system/files/trigger4RP2_v2.pdf, December, 2014.
- [15] R. Sikora, "Naming convention and layout of the Roman Pot Phase II* subsystem in the STAR experiment." https://drupal.star.bnl.gov/STAR/system/files/RomanPotNomenclature_0.pdf, October, 2014.
- [16] http://www.star.bnl.gov/public/comp/prod/DataSummary.html.
- [17] https://drupal.star.bnl.gov/STAR/event/2017/09/27/software-and-computing-meeting/revertexing-2015-rp-stream.
- [18] L. Adamczyk. https://drupal.star.bnl.gov/STAR/system/files/talk_42.pdf, March, 2016.
- [19] https://github.com/rafalsikora/CEP-STAR.
- [20] S. Das, "A simple alternative to the Crystal Ball function," arXiv:1603.08591 [hep-ex].